Volume-averaged modeling of multiphase solidification with equiaxed crystal sedimentation in a steel ingot

Xiao-lei Zhu[1, 2, 3], Shuang Cao[2], Rui Guan[1, 3], **Ji Yang[2], *Zhe Ning[1, 3], Xin-gang Ai[1, 3], Sheng-li Li[1, 3], and Xin-cheng Miao[3]

1. The key Laboratory of Material Forming and Structure Property Control, Anshan 114051, Liaoning, China

2. State Key Laboratory of Metal Material for Marine Equipment and Application, Anshan 114009, Liaoning, China

3. School of Materials and Metallurgy, University of Science and Technology Liaoning, Anshan 114051, Liaoning, China

Abstract: Macrosegregation is a critical factor that limits the mechanical properties of materials. The impact of equiaxed crystal sedimentation on macrosegregation has been extensively studied, as it plays a significant role in determining the distribution of alloying elements and impurities within a material. To improve macrosegregation in steel connecting shafts, a multiphase solidification model that couples melt flow, heat transfer, microstructure evolution, and solute transport was established based on the volume-averaged Eulerian-Eulerian approach. In this model, the effects of liquid phase, equiaxed crystals, columnar dendrites, and columnar-to-equiaxed transition (CET) during solidification and evolution of microstructure can be considered simultaneously. The sedimentation of equiaxed crystals contributes to negative macrosegregation, where regions between columnar dendrites and equiaxed crystals undergo significant A-type positive macrosegregation due to the CET. Additionally, noticeable positive macrosegregation occurs in the area of final solidification in the ingot. The improvement in macrosegregation is beneficial for enhancing the mechanical properties of connecting shafts. To mitigate the thermal convection of molten steel resulting from excessive superheating, reducing the superheating during casting without employing external fields or altering the design of the ingot mold is indeed an effective approach to control macrosegregation.

Keywords: ingot casting; multiphase solidification model; equiaxed crystal sedimentation; microstructure; macrosegregation

CLC numbers: TG142.11/TP391.9   **Document code:** A   **Article ID:** 1672-6421(2024)03-229-10

1 Introduction

The connecting shaft between the support arm and the base is the main bearing part of hydraulic support equipment for mining. As the equipment size increases, manufacturers raise their expectations for the mechanical properties of connecting shafts. During the casting of connecting shafts, macrosegregation hinders the improvement of mechanical properties [1]. The primary mechanism for macrosegregation is the relative movement between solute-enriched melt and solidified dendrites during solidification [2]. Several factors contribute to this relative movement, including thermal solute convection in the melt during solidification [3-5], sedimentation of equiaxed crystals [6,7], thermal shrinkage and solidification shrinkage [8-12], forced convection under a magnetic field [13-16], and shell deformation caused by mechanical reduction [17-19]. However, equiaxed crystal sedimentation is obviously an important factor affecting macrosegregation for ingot casting.

Solute transport with equiaxed crystal sedimentation has been extensively studied. In 1994, Charbon et al. [20] introduced a mathematical model to elucidate the convective flow induced by settlement of equiaxed crystals in small ingots. The effects of equiaxed crystal movement on microstructure, solid/liquid interfacial behavior for eutectic alloys with varying casting parameters were evaluated simultaneously.

*Zhe Ning

Ph.D. His research interests mainly focus on metallurgical reaction engineering and physico-chemistry of process metallurgy.

E-mail: classal@126.com

**Ji Yang

E-mail: baiyuncanggou1992@aliyun.com

Subsequently, they developed a two-phase solidification model that incorporated convective flow and equiaxed crystal settlement to predict microstructure and macrosegregation in ingots. Their findings indicated that equiaxed crystal settlement could result in negative macrosegregation at the bottom of the ingot, while it influenced positive macrosegregation in the upper part of the ingot. Based on the Eulerian approach, Zhang et al. [7] used a two-phase model to simulate the solidification of an ingot. In this model, equiaxed crystal nucleation, microstructure evolution, grain/crystal dissociation, precipitation, melt convection, and solute transport were fully considered. They found that the movement of equiaxed crystals significantly affected melt flow and solidification, and the settlement of spherical equiaxed crystals was the main reason for negative segregation. In 2009, Combeau et al. [23] developed a multiphase model to describe the microstructure evolution and movement of equiaxed crystals. This model fully considered melt flow between dendrites, blocked crystal migration, and equiaxed crystal movement in the ingot and analyzed the corresponding microstructure and macrosegregation. Recently, Zhang et al. [24] used a two-phase solidification model to study the nucleation and remelting of equiaxed crystals. The mechanism of solute and energy transport plays a crucial role in determining the heterogeneity of microstructure and element distribution during solidification. Studying this mechanism can further enhance our understanding of equiaxed crystal nucleation, dendrite remelting, and fragmentation. However, it is important to note that considering only equiaxed crystal migration during solidification is not sufficient for a comprehensive understanding. The influences of columnar dendrites and columnar-to-equiaxed (CET) on macrosegregation have not been extensively studied in the context of equiaxed crystal sedimentation theory. This emphasizes the need for systematic research to comprehensively understand how these factors influence macrosegregation during solidification.

In this study, an Eulerian-Eulerian multiphase solidification model that couples melt flow, heat transfer, microstructure evolution, and solute transport was developed based on the finite volume method. In this model, the effects of the liquid phase, equiaxed crystal, columnar dendrite, and CET during solidification on the evolution of microstructure were considered simultaneously. Finally, to validate this multiphase solidification model, macrosegregation was verified by using infrared carbon-sulfur analysis.

2 Model description

An Eulerian-Eulerian multiphase solidification model was developed based on the finite volume method. One of the major advantages of this model is its ability to separately solve the transport equations for different phases. By considering equiaxed crystal sedimentation, the model allows for simultaneous calculation of conservation equations involving mass, momentum, energy, and species transfers during the solidification process.

2.1 General assumption

To better use mathematical equations to characterize the complex solidification phenomenon described above, certain assumptions about the physical phenomena were presented as follows:

(1) The characters of f_l, f_e, and f_c represented the volume fractions of different phases: the liquid phase (f_l), equiaxed crystals (f_e), and columnar dendrites (f_c). The sum of the volume fractions for all phases was 1 [24].

(2) To achieve local thermal equilibrium at lower melt velocities and ensure sufficient heat exchange between each phase, a larger diffusional heat exchange coefficient ($H^*=10^8$) was employed to facilitate temperature balancing among the phases [25].

(3) Elements such as Si, Mn, P, and S exhibit segregation behavior similar to that of carbon (C) on a macroscopic scale [26, 27]. Because the equilibrium distribution coefficients of these elements are less than 1, solute enrichment occurs in the liquid phase, leading to the formation of positive macrosegregation [28]. Consequently, in the multiphase solidification model, only carbon was considered.

(4) To give some physical properties to columnar dendrites and equiaxed crystals in solidified microstructures, the primary columnar dendrites were assumed to be cylindrical, and the equiaxed crystals were assumed to be spherical [29].

2.2 Mass conservation

The Eulerian-Eulerian volume-averaged mass conservation equations for each phase are as follows [30]:

$$\frac{\partial\left(\rho_l f_l\right)}{\partial t} + \nabla \cdot \left(f_l \rho_l \vec{v}_l\right) = -S_{le} - S_{lc} \tag{1}$$

$$\frac{\partial\left(\rho_c f_c\right)}{\partial t} + \nabla \cdot \left(f_c \rho_c \vec{v}_c\right) = -S_{lc} - S_{ce} \tag{2}$$

$$\frac{\partial\left(\rho_e f_e\right)}{\partial t} + \nabla \cdot \left(f_e \rho_e \vec{v}_e\right) = -S_{le} + S_{ce} \tag{3}$$

where ρ_l, ρ_e, and ρ_c are the densities of the liquid phase, equiaxed crystal, and columnar dendrite, respectively; $\vec{v}_l$, $\vec{v}_e$, and $\vec{v}_c$ are the velocity vectors of the liquid phase, equiaxed crystal, and columnar dendrite, respectively; S_{ce} represents the columnar-equiaxed net mass transfer rate S_{le} represents the liquid-equiaxed net mass transfer rate; and S_{lc} represents the liquid-columnar net mass transfer rate, which can be calculated by Eqs. (4) and (5) [31]:

$$S_{le} = v_e' A_e' \rho_e = \left(I_s^e v_e\right)\left(n_e 4\pi R_e^2 f_l\right)\rho_e \tag{4}$$

$$S_{lc} = v_c' A_c' \rho_c + i\vec{S}_c' = \left(I_s^c v_c^{sec}\right)\left(2\pi R_c f_l / \lambda_1^2\right)\rho_c \\ + i v_c^{pri} n_c \pi R_c' \rho_c f_l \tag{5}$$

In Eq. (4), the interfacial growth rate of the equiaxed crystal envelop (v_e') and the growth rate of the dendritic tip (v_e) of anequiaxed crystal can be calculated using the Lipton-Glicksman-Kurz (LGK) model [32]. A_e' represents the area

concentration of the equiaxed crystal. I_s^e is the influencing factor of the crystal outline, equal to 0.683. n_e is the nucleation density, and R_e is the radius of the equiaxed crystal. In Eq. (5), v_c^{pri} and v_c^{sec} represent the growth velocities of the dendritic tip of the primary dendrite and secondary dendrite, which can be calculated by the Kurz-Giovanola-Trivedi (KGT) [33] and LGK models, respectively. A_c' denotes the area concentration of the columnar dendrite. Shape factor I_s^c is equal to 0.7979. R_c and R_c' are the radii of the columnar dendrite arm and columnar dendrite tip, respectively. λ_1 represents the primary dendrite arm spacing. i is state index, which can be used to mark different phases. n_e and n_c are the densities of equiaxed crystal and columnar dendrite. $\vec{S}_c'$ is the mass transfer rate at the front of columnar dendrite tip.

2.3 Momentum conservation

To describe the melt flow in the calculation domain, the Navier-Stokes equations were used [33]:

$$
\frac{\partial}{\partial t}\left(f_1\rho_1\vec{v}_1\right) + \nabla\cdot\left(f_1\rho_1\vec{v}_1\vec{v}_1\right) = -f_1\nabla P
$$
$$
+ \nabla\cdot\left(f_1\left(\mu_1 + \mu_{t,k}\right)\left(\nabla\vec{v}_1 + \left(\nabla\vec{v}_1\right)^T\right)\right) + \vec{F}_T^1 + \vec{F}_C^1 + \vec{V}_{cl} + \vec{V}_{el} \quad (6)
$$

$$
\frac{\partial}{\partial t}\left(f_e\rho_e\vec{v}_e\right) + \nabla\cdot\left(f_e\rho_e\vec{v}_e\vec{v}_e\right) = -f_e\nabla P + \nabla\cdot\left(f_e\left(\mu_e + \mu_{t,k}\right)\right.
$$
$$
\left.\left(\nabla\vec{v}_e + \left(\nabla\vec{v}_e\right)^T\right)\right) + \vec{F}_T^e + \vec{F}_C^e + \vec{F}_u + \vec{V}_{le} + \vec{V}_{ce} \quad (7)
$$

where P is the pressure, μ_1 and μ_e are the viscosities of the liquid phase and equiaxed crystal, and $\mu_{t,k}$ is the turbulent viscosity. As the source terms of the Navier-Stokes equations, $\vec{F}_T^1$, $\vec{F}_C^1$, $\vec{F}_T^e$ and $\vec{F}_C^e$ are driving forces related to the thermal buoyancy and solutal buoyancy of the liquid phase and equiaxed crystals; $\vec{F}_u$ is a discriminatory function; and $\vec{V}_{cl}$, $\vec{V}_{ce}$ and $\vec{V}_{el}$ are the momentum transfer source terms between different phases.

2.4 Energy conservation

The heat transfer model was used to ensure energy conservation and investigate the energy transfer between the liquid phase, equiaxed crystals, and columnar dendrites, as follows:

$$
\frac{\partial}{\partial t}\left(f_1\rho_1 H_1\right) + \nabla\cdot\left(f_1\rho_1\vec{v}_1 H_1\right)
$$
$$
= \nabla\cdot\left(f_1 k^*\left(\nabla T_1\right)\right) - H\left(S_{le} + S_{lc}\right) - H^*\left(2T_1 - T_e - T_c\right) \quad (8)
$$

$$
\frac{\partial}{\partial t}\left(f_e\rho_e H_e\right) + \nabla\cdot\left(f_e\rho_e\vec{v}_e H_e\right)
$$
$$
= \nabla\cdot\left(f_e k^*\left(\nabla T_e\right)\right) + HS_{le} + H^*\left(T_1 - T_e\right) \quad (9)
$$

$$
\frac{\partial}{\partial t}\left(f_c\rho_c H_c\right) + \nabla\cdot\left(f_c\rho_c\vec{v}_c H_c\right)
$$
$$
= \nabla\cdot\left(f_c k^*\left(\nabla T_c\right)\right) + HS_{lc} + H^*\left(T_1 - T_c\right) \quad (10)
$$

where T_1, T_e, and T_c are the temperatures of liquid phase, equiaxed crystal, and columnar dendrites, and H_1, H_e, and H_c

are the enthalpies of the liquid phase, equiaxed crystals, and columnar dendrites, k^* is the effective thermal conductivity [34], and H is the phase transition enthalpy.

2.5 Species conservation equations

The species conservation equations are as follows [35]:

$$
\frac{\partial\left(\rho_1 f_1 c_1\right)}{\partial t} + \nabla\cdot\left(f_1\rho_1\vec{v}_1 c_1\right) = -C_{le}^P - C_{le}^D - C_{lc}^P - C_{lc}^D \quad (11)
$$

$$
\frac{\partial\left(\rho_e f_e c_e\right)}{\partial t} + \nabla\cdot\left(f_e\rho_e\vec{v}_e c_e\right) = C_{le}^P + C_{le}^D + C_{ce}^P + C_{ce}^D \quad (12)
$$

$$
\frac{\partial\left(\rho_c f_c c_c\right)}{\partial t} + \nabla\cdot\left(f_c\rho_c\vec{v}_c c_c\right) = C_{lc}^P + C_{lc}^D + C_{le}^P + C_{le}^D \quad (13)
$$

where c_1, c_e, and c_c are the solute concentrations of the liquid phase, equiaxed crystals, and columnar dendrites, respectively. C_{le}^P, C_{lc}^P, and C_{ce}^P are the source terms of solute transfer equation related to phase transfer, and C_{le}^D, C_{lc}^D, and C_{ce}^D are the source terms of solute transfer equation in connection with diffusion.

Degree of carbon macrosegregation (c_{mix}/c_0) is an important index to evaluate the macrosegregation during solidification of an ingot. The equation for this calculation is as follows [24]:

$$
\frac{c_{mix}}{c_0} = \frac{\rho_1 f_1 c_1 + \rho_e f_e c_e + \rho_c f_c c_c}{\left(\rho_1 f_1 + \rho_e f_e + \rho_c f_c\right)\cdot c_0} \quad (14)
$$

where c_{mix} is the mass fraction of carbon according to the mixture theory, and c_0 is the initial carbon mass fraction.

2.6 Dendrite growth kinetics

Based on the cellular automata (CA) principle [36], a dynamic growth model of columnar dendrites was established, and the equiaxed crystal distribution was defined using the Kernel density estimation (KDE) model [37]. When the columnar dendrites grow from the surface to the center of the calculation domain, the growth rate of the whole dendrite depends on the growth rate of the columnar dendrite tip. However, the preferred direction of the crystal was not considered when calculating the growth rate of the columnar dendrite tip. To achieve dynamic tracking of the columnar dendrite tip, the following assumptions were established:

(1) The calculation domain was divided into several volume elements, and each volume element was marked with different indexes (i) during solidification. The index (i) showed whether the volume element contained a columnar dendrite trunk ($i=0$), columnar dendrite tip ($i=1$), or liquid phase and equiaxed crystal ($i=2$). All volume elements were initialized with an index equal to 2 ($i=2$), and the index (i) of each volume element was updated with the microstructure evolution, as shown in Fig. 1.

(2) The size of each volume element was fixed, and the reference length (l_{ref}) was used to control the volume element size. When the columnar dendrite tip entered a volume element, it was necessary for its growth length to be greater than the reference length (l_{ref}) to pass through the
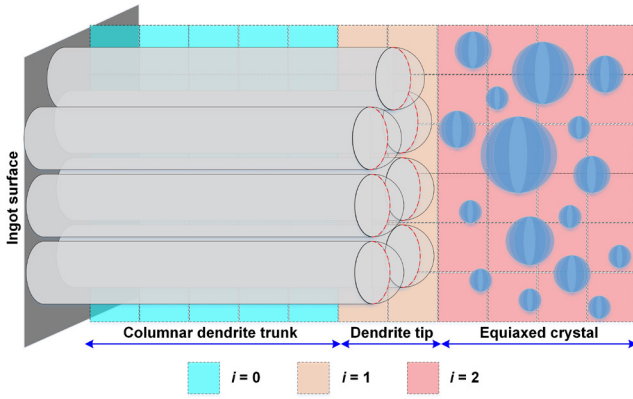
Fig. 1: Schematic diagram of microstructural evolution in multiphase solidification model

corresponding volume element. Therefore, the equivalent spherical surface (ΔS) was used to calculate the reference length of each volume element [$l_{ref}=2(\Delta S/\pi)^{0.5}$].

(3) When the index $i=0$, the corresponding volume element represented the columnar dendrite trunk, and the mass transfer between the high-temperature melt outside the solidified columnar dendrite and the columnar dendrite was artificially terminated.

(4) In this work, the CET at the front of the columnar dendrite tip was considered by referencing "mechanical blocking" from the theory of Hunt [38]. When the local volume fraction (f_e) of the equiaxed crystal exceeded a critical value ($f_e^{CET}=0.49$), the growth rate of the columnar dendrite tip (v_c^{pri}) was set to 0, and then the index of the volume element where the columnar dendrite tip was located was changed to 2.

In the description of microstructure evolution, the dynamic growth models of the columnar dendrite, equiaxed crystal nucleation, and Gaussian distribution model were mainly introduced in this study as follows:

2.6.1 Dynamic growth model of columnar dendrites

The columnar dendrite morphology was simplified as a multilayered cylinder. To precisely simulate columnar dendrite growth, it was necessary to consider the growth velocities of columnar dendrite trunk and columnar dendrite tip. Based on the Kurz-Giovanola-Trivedi (KGT) model [32], the growth rate of the dendrite tip in the dynamic growth model of columnar dendrites can be expressed as follows:

$$v_c^{pri} = a_1 \Delta T^2 + a_2 \Delta T^3 \tag{15}$$

where a_1 and a_2 are fitting coefficients of columnar dendrite growth [16]. ΔT is the undercooling degree of columnar dendrite tip nucleation, which can be calculated by considering the influence of thermal undercooling degree (ΔT_t), component undercooling degree (ΔT_c), and curvature undercooling degree (ΔT_r) simultaneously, as shown in Eq. (16):

$$\Delta T = \Delta T_t + \Delta T_c + \Delta T_r \tag{16}$$

When the growth length of the columnar dendrite tip was greater than the reference length (l_{ref}), the element index was immediately switched to that represented by the columnar dendrite trunk. Therefore, by the differential method, the growth rate of columnar dendrite tip was used to obtain the growth length (l) of the columnar dendrite, and the dynamic tracking of the position of the columnar dendritic tip was also realized. In the dynamic growth model of columnar dendrites, the different forms of columnar dendrite growth length can be expressed by Eq. (17):

$$dl = \left(v_c^{pri} \right) dt \tag{17}$$

2.6.2 Equiaxed crystal nucleation and Gaussian distribution model

In the multiphase solidification model, the conservation equation for calculating equiaxed crystals is as follows:

$$\frac{\partial}{\partial t} n_e + \nabla \cdot \left(\vec{v}_e n_e \right) = N_e \tag{18}$$

where n_e and N_e are the nucleation density and nucleation rate of the equiaxed crystal, respectively. The morphology of the equiaxed crystal was simplified as a sphere in this study, and solute redistribution occurred at the boundary of the spherical crystal. By considering the undercooling (ΔT) of the liquid phase at the front of the solidification interface, the kernel density estimation (KDE) model was used to predict the nucleation rate of equiaxed crystals [37], as shown in Eq. (19):

$$N_e = \frac{d(n_e)}{d(\Delta T)} \cdot \frac{d(\Delta T)}{dt} = \frac{d(\Delta T)}{dt} \frac{n_{max}}{\sqrt{2\pi}\Delta T_\sigma} e^{-0.5\left(\frac{\Delta T - \Delta T_N}{\Delta T_\sigma}\right)^2} \tag{19}$$

where, ΔT_σ and ΔT_N are the standard deviation and average nucleation undercooling, respectively, which can be found in Table 1. n_{max} is the maximum nucleation density of the equiaxed crystal, which is set to 2.224×10^6 in this study.

2.7 Model geometry, experimental parameters, and solution strategy

To reduce the difficulty of the cutting process, the connecting shaft of the mine hydraulic support equipment is made from a cylindrical ingot. The solidification of a cylindrical ingot with a diameter of 130 mm and a height of 460 mm was investigated using Fluent software (ANSYS, Inc., Canonsburg, PA). To reduce computing resources, half of the vertical section of the cylindrical ingot was selected as the calculation domain, as shown in Fig. 2(a). As shown in Fig. 2(b), the boundary conditions of the calculation domain were divided into four regions: the top surface, bottom surface, cooling wall, and axis of symmetry. Because only the static solidification of the ingot was simulated, the velocity boundary condition for the calculation domain was not involved. The detailed boundary conditions for each phase in the multiphase solidification model of heat transfer are given in Table 1.

Based on the Eulerian-Eulerian approach, the conservation equations that couple heat transfer, melt flow, solute transfer, and microstructure evolution in the multiphase solidification model can be solved by using the phase-coupled SIMPLE

Table 1: Detailed boundary conditions of heat transfer used in the simulation

Region	Boundary condition	Heat transfer coefficient
Top surface	Convective	300 W·m^{-2}·K^{-1}
Bottom surface	Convective	800 W·m^{-2}·K^{-1}
Cooling wall	Convective	1,800 W·m^{-2}·K^{-1}
Symmetry axis	Symmetry	Zero-gradient
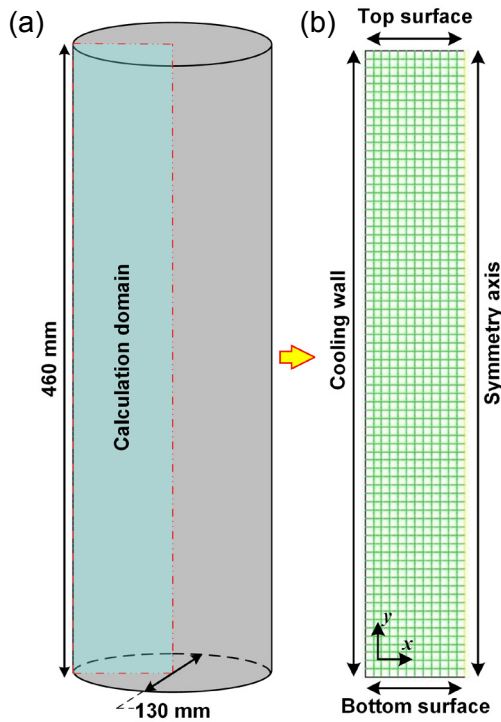
Fig. 2: Schematic representation of the whole calculation domain of geometric model (a) and corresponding mesh (b)

(PC-SIMPLE) algorithm. To reduce the standardized residuals of c_l, c_e, c_c, f_e, f_c, $\vec{v}_l$, $\vec{v}_e$, p, and n_e to less than the convergence limit (10^{-4}) and reduce the standardized residuals of h_l, h_e, and h_c to less than 10^{-7}, the number of iterations in each time step should not exceed 40 at most. When solving the conservation equations, the dynamic growth model of columnar dendrites in the microstructure was executed before each iteration, the position of the columnar dendrite tip was calibrated, and the columnar dendrite growth morphology at the current calculation time was determined. Then, based on the results of the last iteration, the source terms of each conservation equation and the equiaxed crystal nucleation model were solved iteratively. Finally, the conservation equations of mass, momentum, enthalpy, solute transport, and microstructure evolution were solved while the material properties were updated. A detailed flow chart of the calculation of the multiphase solidification model is shown in Fig. 3. The thermophysical properties and process parameters used in the simulation are shown in Table 2.
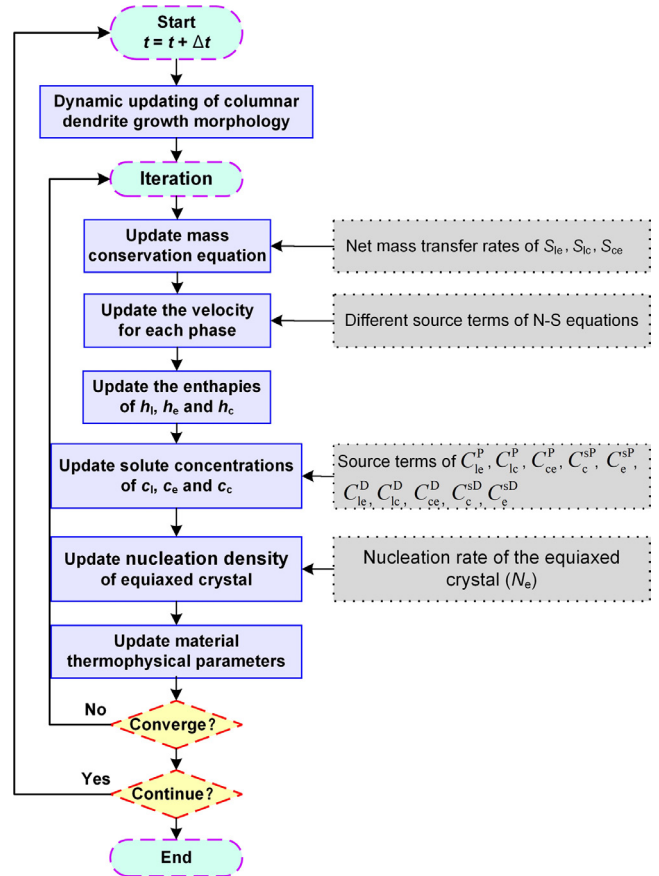

Fig. 3: Flow chart of calculation of the multiphase solidification model

3 Results and discussion

3.1 Distribution of temperature and velocity

In this work, different phases were assigned the same initial and boundary conditions, so, nearly identical temperature and velocity distributions were obtained by the multiphase solidification model. Therefore, only the temperature and velocity distributions of columnar dendrites are shown in Fig. 4. In addition, since the insulating riser was not built in this simulation to feed the shrinkage near the ingot center, the top of the ingot is solidified at first, and the region above the ingot center is solidified at last during the solidification process.

The velocity distribution on the vertical section of the steel ingot for columnar dendrites is also shown in Fig. 4. As the solidification of the steel ingot was simulated in a static state, the forced convection flow with the effect of the external field was not imposed, the liquid phase only had a certain flow velocity under the influence of thermal buoyancy and solute buoyancy. Therefore, it can be seen from the velocity distribution of columnar dendrites that the upper middle part of the ingot has a certain flow velocity, indicating this was the final solidification region of the ingot.

3.2 Microstructure evolution

Figure 5 shows the volume fractions on the vertical section of the steel ingot for different phases, including the liquid phase, columnar dendrites, and equiaxed crystals. Figure 6(a) shows

Table 2: Thermophysical properties and process parameters used in the simulation

Item	Symbol/Unit	Value
Calculation domain size	mm	130×460
Density (liquid/equiaxed/columnar)	ρ_l, ρ_e, ρ_c (kg·m^{-3})	7,109/7,109/7,384
Conductivity (liquid/equiaxed/columnar)	k_l, k_e, k_c (W·m^{-1}·K^{-1})	39/33/33
Specific heat (liquid/solid)	$c_{p(l)}$, $c_{p(s)}$ (J·kg^{-1}·K^{-1})	824.62/660.87
Liquidus slope	m (K·wt·pct^{-1})	–78
Latent heat of fusion	ΔH_m (J·kg^{-1})	272,000
Initial carbon concentration	c_0	0.006
Liquid diffusion coefficient	D_l (m^2·s^{-1})	2×10^{-8}
Partition coefficient	k	0.45
Adjustment factor	β	0.8
Maximum nucleation density	n_{max} (m^{-3})	2.224×10^6
Standard deviation	ΔT_σ (K)	1.5
Average nucleation undercooling	ΔT_N (K)	20

that the liquid phase is only present in the upper middle part of the ingot, which is also the final solidification area of the ingot. The distribution of liquid phase is consistent with that of the flow velocity. In Figs. 5(b) and (c), the columnar dendrites are mainly distributed in the upper middle part and corners of the steel ingot, and the equiaxed crystals are mainly distributed in the lower middle part at the center of the ingot. Figures 5(b) and (c) show that the CET occurs in the regions between the columnar dendrites and equiaxed crystals. In addition, Fig. 5(c) shows that the equiaxed crystals undergo obvious sedimentation during the solidification process, and a central zone of grain sediment forms in the lower-middle part of the ingot.

Figure 6 shows the volume fractions of different phases along the centerline of the vertical section of the steel ingot. The phase fractions of columnar dendrites and equiaxed crystals are interdependent and alternate along the centerline of the steel ingot. Especially for the lower middle part of the ingot, the larger volume fraction of equiaxed crystals hinders the further increase in the volume fraction of columnar dendrites.

If the degree of superheating of molten steel could be decreased, it could obviously inhibit the growth of columnar dendrites and expand the areas of equiaxed crystals. When the degree of superheating is high, the melt flow caused by thermal convection will be strengthened. The solute precipitated at the columnar dendrite tips in the early solidification stage will be transferred to the late solidification stage, which will intensify macrosegregation in the center of the steel ingot. Therefore, to reduce macrosegregation in steel ingots, a simple method is to reduce the degree of superheating during the casting process without applying an external field and changing the design of the ingot mold.
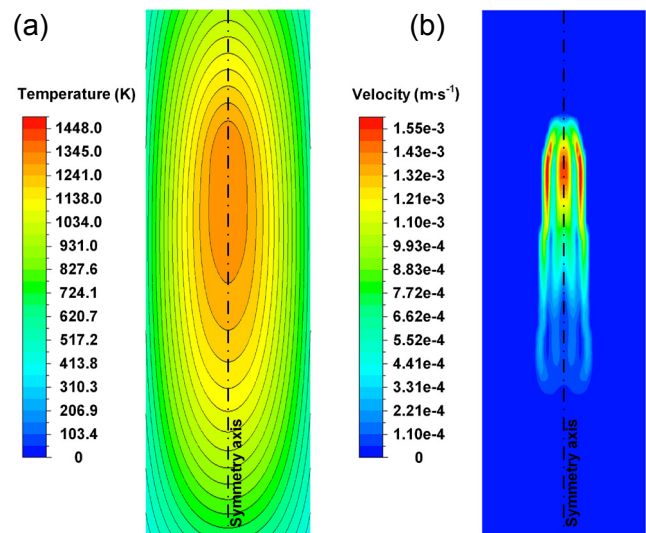

Fig. 4: Distributions of temperature (a) and velocity (b) on vertical section of the steel ingot for columnar dendrites

3.3 Mechanism of macrosegregation

Figure 7 shows the solute distributions of C on the vertical section of the steel ingot for different phases. The multiphase solidification model accurately calculated the solute concentrations for different phases, as shown in Fig. 8. However, the distribution of solute concentration in the whole ingot could not be calculated according to the solute concentration of one single phase. Combined with the volume fraction for each phase shown in Fig. 6, the distribution of solute concentration in the whole ingot should be obtained by the mixture theory. As shown in Fig. 8, it is obvious that for the liquid phase, the
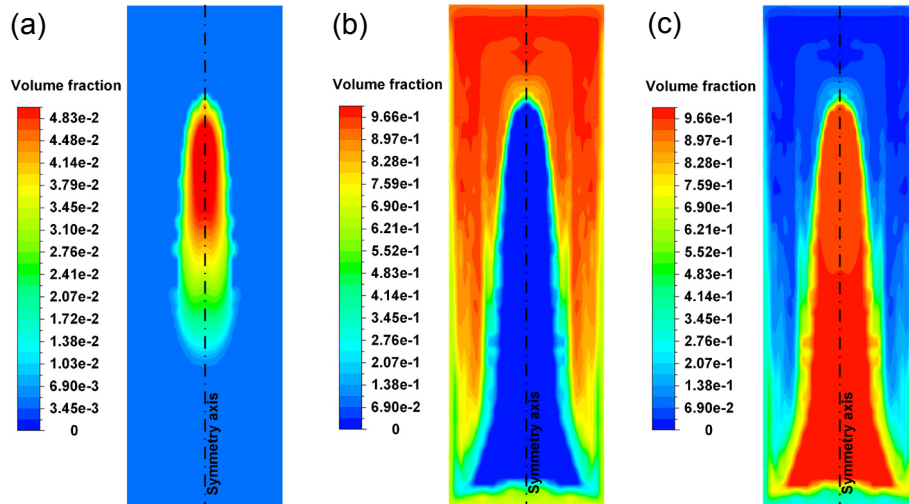
Fig. 5: Volume fractions of different phases on vertical section of steel ingot: (a) liquid; (b) columnar dendrite; and (c) equiaxed crystal
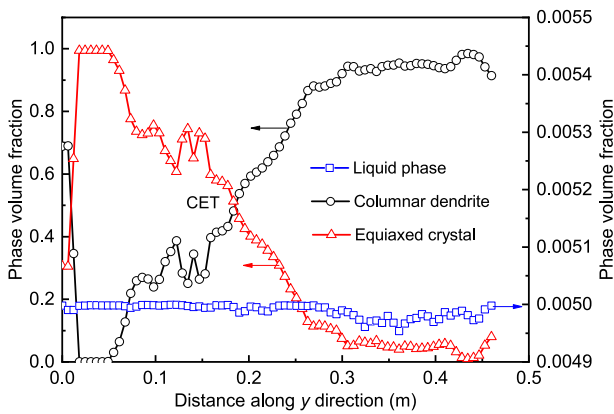

Fig. 6: Volume fractions of phases along the centerline of vertical section of the steel ingot: (a) liquid; (b) columnar dendrite; and (c) equiaxed crystal

solute concentration of the equiaxed crystal region is higher in the lower middle part of the ingot. However, because the fraction of the liquid phase is too low, the solute concentration of C in the liquid phase could not represent the solute

concentration of the whole ingot.

Figure 9 shows a comparison between the calculated and measured degree of macrosegregation (c_{mix}/c_0) on a vertical section of the steel ingot. In Fig. 9(a), the sedimentation of equiaxed crystals causes negative macrosegregation in the lower-middle part of the ingot, while significant A-type positive macrosegregation appears between the distribution regions of columnar dendrites and equiaxed crystals due to the CET. At the front of the solidification interface near the columnar dendrite tip, factors including the occurrence of CET behavior, the changes of solidification conditions, and the enrichment of solute element result in the flow of the liquid phase between equiaxed crystals in the microchannels generated by the local solidification shrinkage, thus A-type macrosegregation occurs. In the upper-middle part of the ingot, that is, the final solidification area of the ingot, obvious positive macrosegregation is formed. Most of the solute enriched liquid phase at the front of the solidification interface eventually converges in the final solidification area and produces severe positive macrosegregation. Compared with the etched macrostructure on the vertical section of the steel ingot shown
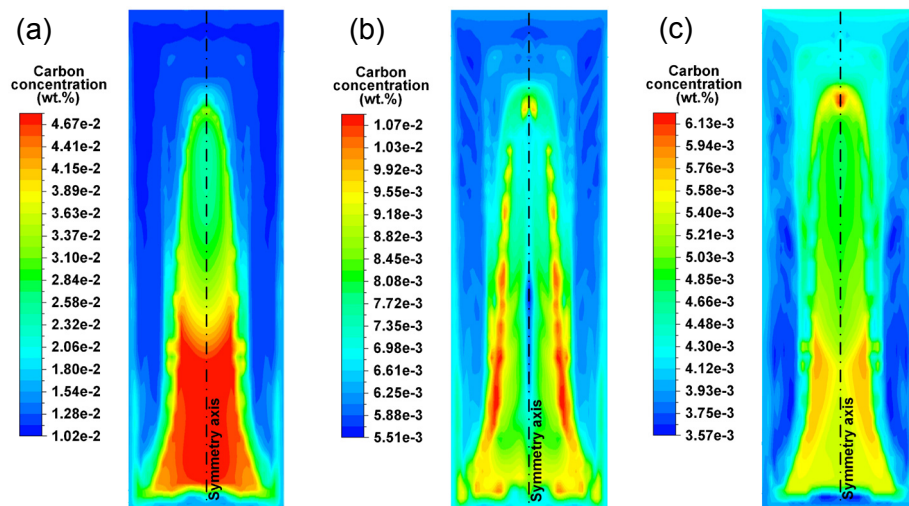

Fig. 7: Solute distributions of C on vertical section of steel ingot for different phases: (a) liquid; (b) columnar dendrite; and (c) equiaxed crystal

in Fig. 9(b), the calculated results for positive macrosegregation in the final solidification area are consistent with the measured results. For the area of equiaxed crystal sedimentation in the lower-middle part of the ingot, the calculated results are also in better agreement with the measured results.

During the solidification of the steel ingot, columnar dendrites grow perpendicular to the ingot surface toward the central liquid phase zone. As the temperature in the mushy zone continuously decreases, undercooling occurs at the columnar dendrite tip, and equiaxed crystals nucleate and grow at the front of the columnar dendrite tip. Due to the difference in the densities of the solid and liquid phases of steel and the free movement of equiaxed crystals formed in the liquid phase, equiaxed crystals gradually precipitate under the effect of gravity. At this point, the sedimentation of equiaxed crystals changes the time when the CET occurs, causing a shift in the position of final solidification. A schematic diagram of the sedimentation of equiaxed crystals in the vertical section of the steel ingot due to the effect of gravity is shown in Fig. 10.
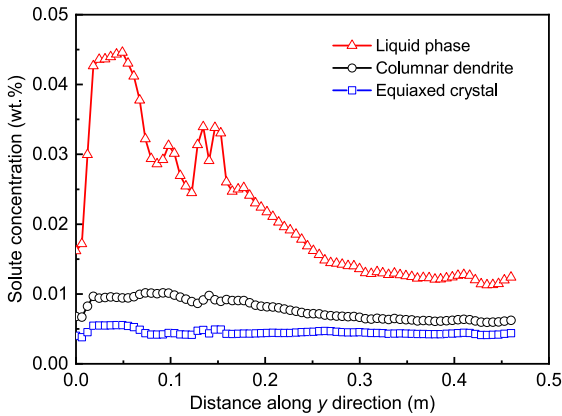
In Fig. 10, under the effect of equiaxed crystal sedimentation, equiaxed crystals aggregate in the middle and lower parts of the steel ingot. This results in a significantly larger volume fraction of equiaxed crystals, while the volume fraction of equiaxed crystals in the upper part of the steel ingot decreases. When the volume fraction of equiaxed crystals near the columnar dendrite tip reaches the critical condition for CET, the growth of columnar dendrites stops, and only equiaxed crystals continue to nucleate and grow. However, if the volume fraction of equiaxed crystals near the tip of the columnar dendrite is low and the critical condition for CET has not been reached, the growth of columnar dendrites persists throughout the solidification process. This mechanism illustrates how the microstructure during solidification is influenced by the sedimentation of equiaxed crystals.

When solute poor equiaxed crystals deposit in the lower part of the steel ingot, the solute enriched liquid phase at the tip of the columnar dendrites around this area will accordingly flow with the equiaxed crystals. Therefore, due to the thermal buoyancy and solute buoyancy, negative macrosegregation occurs in the area of equiaxed crystal sedimentation at the middle and lower parts of the steel ingot, and positive macrosegregation appears at the upper part of the steel ingot.

3.4 Measurement results and model validation

Figure 11(a) shows the various positions and sizes of samples collected for measuring the degree of macrosegregation. To perform infrared carbon-sulfur analysis, 13 spots along the centerline of the vertical section of the steel ingot were drilled

Fig. 8: Solute concentrations of C along centerline of vertical section of steel ingot for different phases: (a) liquid; (b) columnar dendrite; and (c) equiaxed crystal
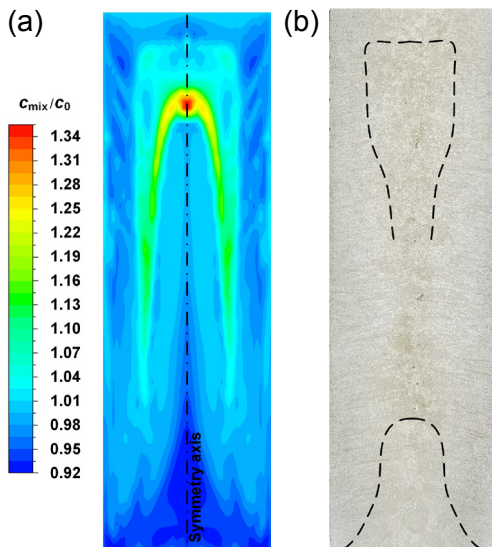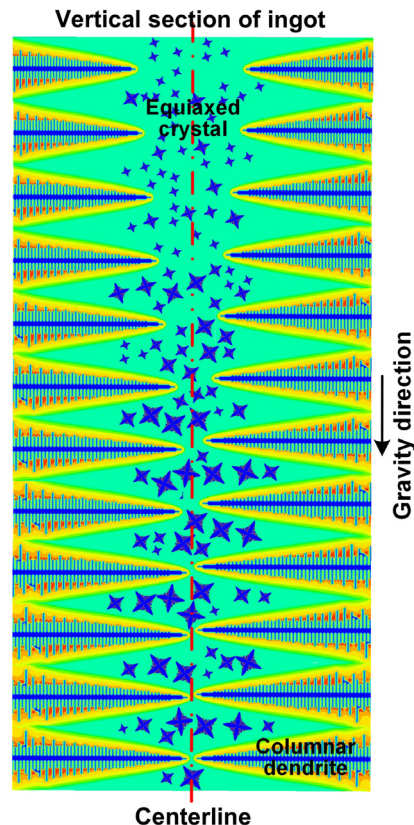

Fig. 9: Comparison between calculated (a) and measured (b) degree of macrosegregation (c_{mix}/c_0) on vertical section of steel ingot

Fig. 10: Schematic diagram of sedimentation of equiaxed crystals in a vertical section of steel ingot

using a drill bit with a diameter of 4 mm. Figure 11(b) shows the measured and calculated degrees of carbon macrosegregation. The overall trends of the measured and calculated degrees of macrosegregation are similar, which prove that the results of the calculation using the multiphase solidification model are accurate.
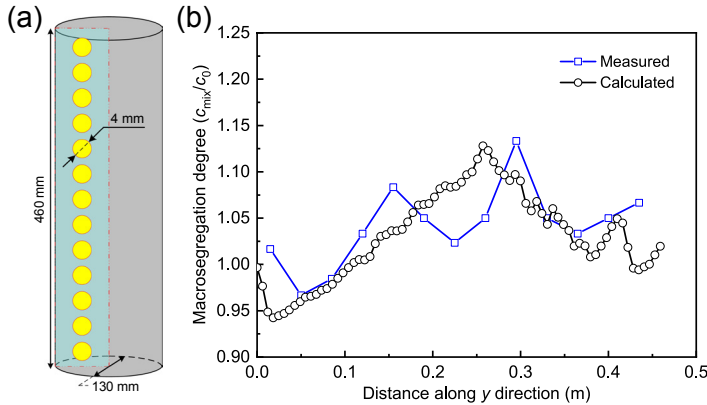

Fig. 11: A schematic diagram of samples (a) and the measured and calculated degrees of carbon macrosegregation along centerline of a vertical section of the steel ingot (b)

4 Conclusions

In this study, a multiphase solidification model based on the Eulerian-Eulerian approach was used to investigate solidification and equiaxed crystal sedimentation in a steel ingot. The main conclusions are summarized as follows:

(1) The temperature distributions of the liquid phase, columnar dendrites, and equiaxed crystals are almost identical because the boundary conditions of different phases are the same in the multiphase solidification model. In addition, under the effects of thermal buoyancy and solute buoyancy, the liquid phase only has a certain flow velocity in the upper middle part of the ingot, which represents the final solidification region of the ingot.

(2) The columnar-to-equiaxed transition mainly occurs in the regions between the columnar dendrites and equiaxed crystals. Equiaxed crystals undergo obvious sedimentation during the solidification process, and a central fine-grained sediment zone forms in the lower middle part of the ingot.

(3) The sedimentation of equiaxed crystals causes negative macrosegregation. Significant A-type positive macrosegregation appears between the columnar dendrites and equiaxed crystals regions due to the columnar-to-equiaxed transition. Obvious positive macrosegregation occurs in the area of final solidification in the ingot.

(4) The calculated results for macrosegregation on the vertical section of the steel ingot are consistent with the measured ones. This agreement proves that the multiphase solidification model used in this study is accurate.

Acknowledgments

Conflict of interest

The authors declare that they have no known competing financial interests or personal relationships that could have appeared to influence the work reported in this paper.

References

[1] Rezende J, Siquieri R, Emmerich H, et al. Prediction of microstructure and microsegregation in a Fe-Mn-C austenitic steel based on phase-field microstructure simulations. Steel Research International, 2009, 80: 609–615.

[2] Ludwig A, Wu M, Abdellah K. On macrosegregation. Metallurgical and Materials Transactions: A, 2015, 46: 4854–4867.

[3] Huppet H E, Worster M G. Dynamic solidification of a binary melt. Nature, 1985, 314: 703–707.

[4] Aboutalebi M R, Hasan M, Guthrie R I L. Coupled turbulent flow, heat, and solute transport in continuous casting processes. Metallurgical and Materials Transactions: B, 1995, 26: 731–744.

[5] Sun H, Zhang J. Study on the macrosegregation behavior for the bloom continuous casting: Model development and validation. Metallurgical and Materials Transactions: B, 2014, 45: 1133–1149.

[6] Wang C Y, Beckermann C. Equiaxed dendritic solidification with convection: Part II. Numerical simulations for an Al-4 Wt pct Cu alloy. Metallurgical and Materials Transactions: A, 1996, 27: 2765–2783.

[7] Zhang H, Wu M, Schumacher P, et al. Modelling melting and grain destruction phenomena during globular equiaxed solidification. Applied Mathematical Modelling, 2021, 97: 821–838.

[8] Raihle C M, Fredriksson H. On the formation of pipes and centerline segregates in continuously cast billets. Metallurgical and Materials Transactions: B, 1994, 25: 123–133.

[9] El-Bealy M. Modeling of interdendritic strain and macrosegregation for dendritic solidification processes: Part I. Theory and experiments. Metallurgical and Materials Transactions: B, 2000, 31: 331–343.

[10] Mehrabian R, Keane M, Flemings C M. Interdendritic fluid flow and macrosegregation: Influence of gravity. Metallurgical and Materials Transactions: B, 1970, 5: 1209–1220.

[11] Xu D, Bai Y, Guo J, et al. Numerical simulation of heat, mass and momentum transport behaviours in directionally solidifying alloy castings under electromagnetic fields using an extended direct-SIMPLE scheme. International Journal for Numerical Methods in Fluids, 2004, 46: 767–791.

[12] Wang T M, Cai S W, Xu J, et al. Continuous casting mould for square steel billet optimized by solidification shrinkage simulation. Ironmaking & Steelmaking, 2010, 37: 341–346.

[13] Zhao J, Cheng Y, Han K, et al. Numerical and experimental studies of surface-pulsed magneto-oscillation on solidification. Journal of Materials Processing Technology, 2016, 229: 286–293.

[14] Wu H, Wei N, Bao Y, et al. Effect of M-EMS on the solidification structure of a steel billet. International Journal of Minerals, Metallurgy, and Materials, 2011, 18: 159–164.

[15] Yu H Q, Zhu M Y. Influence of electromagnetic stirring on transport phenomena in round billet continuous casting mould and macrostructure of high carbon steel billet. Ironmaking & Steelmaking, 2012, 39: 574–584.

[16] Hou Z, Jiang F, Cheng G. Solidification structure and compactness degree of central equiaxed grain zone in continuous casting billet using cellular automaton-finite element method. ISIJ International, 2012, 52: 1301–1309.

[17] Wu M H, Domitner J. Using a two-phase columnar solidification model to study the principle of mechanical soft reduction in slab casting. Metallurgical and Materials Transactions: A, 2012, 43: 945–964.

[18] Dong Q, Zhang J, Wang B, et al. Shrinkage porosity and its alleviation by heavy reduction in continuously cast strand. Journal of Materials Processing Technology, 2016, 238: 81–88.

[19] Ji C, Wu H C, Zhu M Y. Thermo-mechanical behavior of the continuous casting bloom in the heavy reduction process. JOM, 2016, 68: 3107–3115.

[20] Charbon C, Jacot A, Rappaz M. 3D stochastic modelling of equiaxed solidification in the presence of grain movement. Acta Metallurgica et Materialia, 1994, 42: 3953–3966.

[21] Wang C Y, Beckerman C. Equiaxed dendritic solidification with convection: Part II. Numerical simulations for an Al-4 Wt pct Cu alloy. Metallurgical and Materials Transactions: A, 1996, 27: 2765–2783.

[22] Wu M, Ludwig A, Bührig-Polaczek A, et al. Influence of convection and grain movement on globular equiaxed solidification. International Journal of Heat and Mass Transfer, 2003, 46: 2819–2832.

[23] Combeau H, Založnik M, Hans S, et al. Prediction of macrosegregation in steel ingots: Influence of the motion and the morphology of equiaxed grains. Metallurgical and Materials Transactions: B, 2009, 40: 289–304.

[24] Zhang H, Wu M, Rodrigues C M G, et al. Dendrite fragmentation mechanism under forced convection condition by rotating magnetic field during unidirectional solidification of AlSi7 alloy. Acta Materialia, 2022, 241: 118391.

[25] Ludwig A, Wu M. Modeling of globular equiaxed solidification with a two-phase approach. Metallurgical and Materials Transactions: A, 2002, 33: 3673–3683.

[26] Schneider M C, Beckerman C. Simulation of micro-macrosegregation during the solidification of a low-alloy steel. ISIJ International, 1995, 35: 665–672.

[27] Guan R, Ji C, Chen T C, et al. Formation mechanism of abnormal martensite in the welded joint of the bainitic rail. Metallurgical and Materials Transactions: B, 2021, 52, 3220–3234.

[28] Gui L, Long M, Chen D, et al. Thermodynamic study on the solute partition coefficients on L/δ and L/δ+γ phase interfaces for 1215 high-sulfur steel solidification by orthogonal design. Journal of Materials Research and Technology, 2020, 9(1): 89–103.

[29] Mu M, Fjeld A, Ludwig A. Modelling mixed columnar-equiaxed solidification with melt convection and grain sedimentation – Part I: Model description. Computational Materials Science, 2010, 50: 32–42.

[30] Guan R, Ji C, Wu C H, et al. Numerical modelling of fluid flow and macrosegregation in a continuous casting slab with asymmetrical bulging and mechanical reduction. International Journal of Heat and Mass Transfer, 2019, 141: 503–516.

[31] Guan R, Ji C, Zhu M Y. Modeling the effect of combined electromagnetic stirring modes on macrosegregation in continuous casting blooms. Metallurgical and Materials Transactions: B, 2020, 51: 1137–1153.

[32] Lipton J, Glicksman M E, Kurz W. Dendritic growth into undercooled alloy metals. Materials Science and Engineering, 1984, 65: 57–63.

[33] Kurz W, Giovanola B, Trivedi R. Theory of microstructural development during rapid solidification. Acta Metallurgica, 1986, 34: 823–830.

[34] Poole G M, Heyen M, Nastac L, et al. Numerical modeling of macrosegregation in binary alloys solidifying in the presence of electromagnetic stirring. Metallurgical and Materials Transactions: B, 2014, 45: 1834–1841.

[35] Wu M, Ludwig A. Modeling equiaxed solidification with melt convection and grain sedimentation – I: Model description. Acta Materialia, 2009, 57: 5621–5631.

[36] Wang W, Luo S, Zhu M Y. Numerical simulation of three-dimensional dendritic growth of alloy: Part II – Model application to Fe-0.82WtPctC alloy. Metallurgical and Materials Transactions: A, 2016, 47(3): 1355–1366.

[37] Jiang D, Zhu M Y. Solidification structure and macrosegregation of billet continuous casting process with dual electromagnetic stirrings in mold and final stage of solidification: A numerical study. Metallurgical and Materials Transactions: B, 2016, 47: 3446–3458.

[38] Hunt J D. Steady state columnar and equiaxed growth of dendrites and eutectic. Materials Science and Engineering, 1984, 65: 75–83.